Elucidating the Phase Transformation of Li$_4$Ti$_5$O$_{12}$ Lithiation at the Nanoscale

Michael G. Verde,[*][†] Loïc Baggetto,[‡][⊥] Nina Balke,[§] Gabriel M. Veith,[‡] Joon Kyo Seo,[∥] Ziying Wang,[†] and Ying Shirley Meng[*][†]

[†]Department of NanoEngineering, University of California San Diego, La Jolla, California 92093, United States
[‡]Materials Science and Technology Division, Oak Ridge National Laboratory, Oak Ridge, Tennessee 37831, United States
[§]The Center for Nanophase Materials Sciences, Oak Ridge National Laboratory, Oak Ridge, Tennessee 37831, United States
[∥]Materials Science & Engineering Program, University of California San Diego, La Jolla, California 92093, United States

S *Supporting Information*
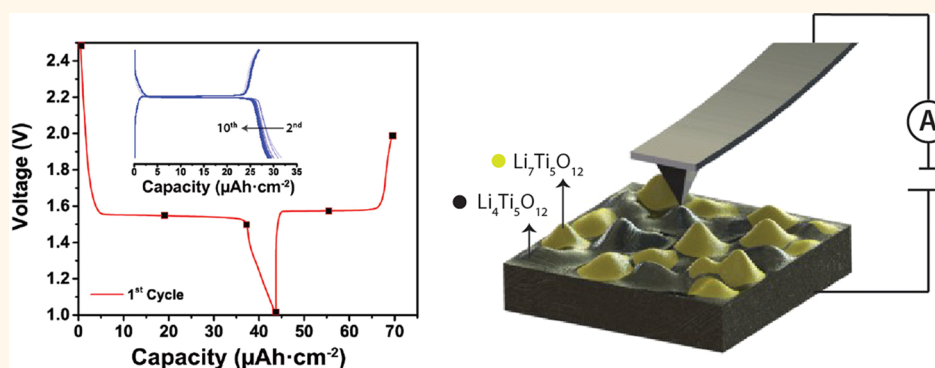
ABSTRACT: This work provides insight regarding the fundamental lithiation and delithiation mechanism of the popular lithium ion battery anode material, Li$_4$Ti$_5$O$_{12}$ (LTO). Our results quantify the extent of reaction between Li$_4$Ti$_5$O$_{12}$ and Li$_7$Ti$_5$O$_{12}$ at the nanoscale, during the first cycle. Lithium titanate's discharge (lithiation) and charge (delithiation) reactions are notoriously difficult to characterize due to the *zero-strain* transition occurring between the end members Li$_4$Ti$_5$O$_{12}$ and Li$_7$Ti$_5$O$_{12}$. Interestingly, however, the latter compound is electronically conductive, while the former is an insulator. We take advantage of this critical property difference by using conductive atomic force microscopy (c-AFM) to locally monitor the phase transition between the two structures at various states of charge. To do so, we perform *ex situ* characterization on electrochemically cycled LTO thin-films that are never exposed to air. We provide direct confirmation of the manner in which the reaction occurs, which proceeds *via* percolation channels within single grains. We complement scanning probe analyses with an X-ray photoelectron spectroscopy (XPS) study that identifies and explains changes in the LTO surface structure and composition. In addition, we provide a computational analysis to describe the unique electronic differences between LTO and its lithiated form.

KEYWORDS: *Li$_4$Ti$_5$O$_{12}$, LTO, Li-ion battery, anode, thin-film, c-AFM, XPS*

D ue to the demand for high energy density batteries for mobile electronics and electric vehicles, the quest for high capacity, low voltage anode materials—especially involving Si—has been heavily pursued in recent years.[1] In this respect, Li$_4$Ti$_5$O$_{12}$ (lithium titanate, LTO) is viewed as an inferior lithium ion battery anode. It exhibits relatively low capacity and high voltage compared to the most commercially available Li-ion anode, graphite (175 *vs* 372 mAh·g^{-1} and 1.55 *vs* ~0.1 V Li/Li$^+$).[2] Nevertheless, the same undesirable properties that contribute to low energy densities provide attractive advantages as well. Indeed, the high redox potential of LTO lies safely within the electrolyte stability window.[3] This enables cycling without the formation of deleterious passivation layers, which are a problem for the long-term stability of conventional graphite anode and the popular alternatives such as silicon.[4] The two-phase reaction, which leads to moderate capacity, is also highly facile. It proceeds between two members (Li$_4$Ti$_5$O$_{12}$ and Li$_7$Ti$_5$O$_{12}$) that possess the same crystallographic space group, $Fd\overline{3}m$. Even upon intercalation of 3 Li$^+$ per formula unit, there is only a 0.2% volume change of the spinel lattice, resulting in its description as a *zero-strain* material.[5] The
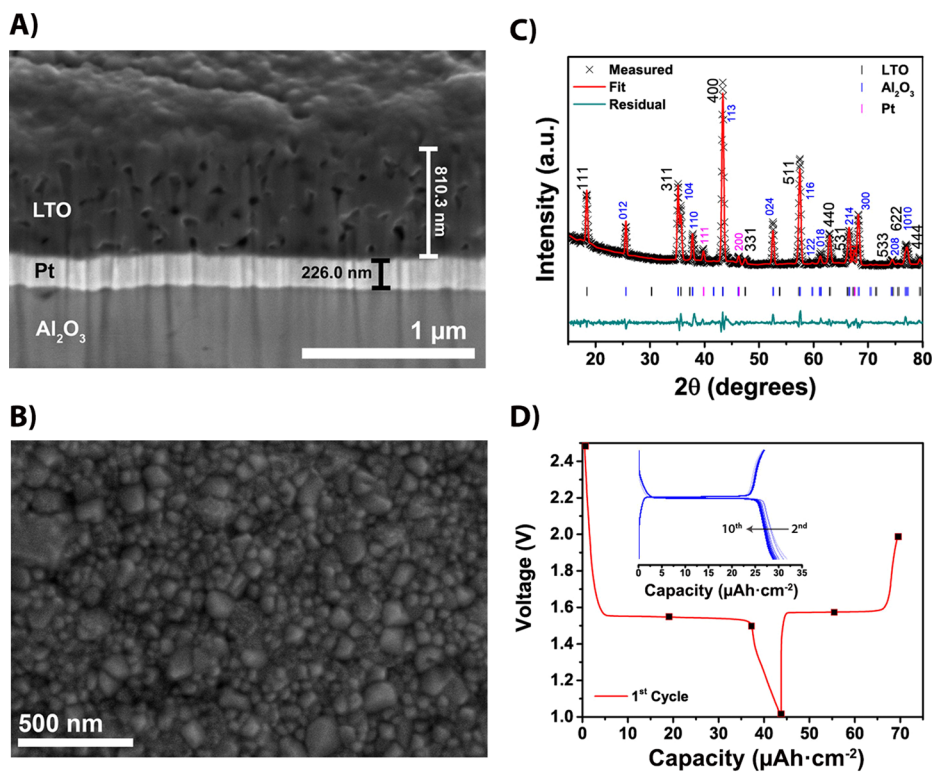
Figure 1. (A) Scanning electron microscopy (SEM) of a focused ion beam (FIB) cross section of the LTO thin-film and (B) top SEM image of the bare thin-film. Note that in (A) the top layer is a protective film used during FIB milling. (C) XRD pattern and Rietveld refinement of LTO thin film deposited onto Pt coated Al_2O_3 substrate. (D) Electrochemical profile of first cycle, with squares indicating points where samples were characterized, and first 10 cycles (inset).

stability, robustness, and safety of LTO have in fact led to its successful commercialization.[6]

While the ionic conductivity of LTO is comparable to that of other Li-ion anodes, a major shortcoming is its inherently low electronic conductivity.[7−10] $Li_4Ti_5O_{12}$ is considered to be an insulator, with experimentally reported band gaps typically between 3.0 and 4.0 eV.[11,12] To circumvent this problem, several strategies have been implemented. Coatings, such as carbon, have been applied to improve the electronic conductivity.[13] Doping with a host of cations has also been performed to decrease the band gap and improve performance.[14−16] Alternatively, LTO nanostructures have been synthesized to shorten Li^+ diffusion lengths and increase surface areas.[17] The high surface area of nanoparticles typically promote two-phase reactions to proceed in order to minimize the large interface energy that would otherwise exist within small volume particles.[18] When these treatments have been applied, extremely high reversible rates of up to 100C (full charge or discharge in almost 30 s) have been reported.[19−21] Other work by Song et al. showed that even pristine LTO could be cycled fairly well without any form of modification.[22] Kim et al. used an array of electrochemical and spectroscopic techniques to propose a mechanism responsible for this.[23] Their hypotheses ultimately rest on the fact that LTO's lithiated phase, $Li_7Ti_5O_{12}$, is highly electronically conductive. If a small network of this phase forms upon initial discharge, it can enable an electronic pathway for further lithiation. Indeed, only a small extent of lithiation is required, as Young et al. have shown that at less than 5% capacity, LTO's bulk electronic conductivity dramatically increases from about 10^{-7} to 10^{-1} S· cm^{-1}.[24]

Understanding exactly how the phase transformation between $Li_4Ti_5O_{12}$ and $Li_7Ti_5O_{12}$ proceeds and what factors promote it is still relatively ill-defined. Because the lattice parameters of both structures are near identical, few diffraction techniques are able to physically differentiate them.[25,26] Though rapid changes in bulk conductivity and light absorption have been observed upon minor lithiation, the exact mechanism that enables this is still not clear. The present study aims to exploit the most significant property difference between the two phases, their difference in electronic conductivity, in order to more fully explain the insulator−metal transition occurring within the system. Using conductive atomic force microscopy (c-AFM), we directly visualize the formation and distribution of each phase at the nanoscale, for the first time. We present comprehensive current and topography maps of LTO, at various states of charge, to demonstrate where the transition between these two phases occurs, and what features promote it. We also perform DFT calculations to more fully describe the reaction mechanism and structures formed. The band gaps of LTO and its lithiated form are calculated in order to confirm which phase is observed when conductivity is measured. These results are combined with chemistry-resolved surface measurements using X-ray photoelectron spectroscopy (XPS), at the same states of charge, to explain changes in surface morphology and composition. It is worth emphasizing that this study focuses on thin-film electrodes, which serve as a model system that possesses no binder or additive, in order to draw conclusions regarding the fundamental properties of LTO. The unique application of the scanning probe microscopy (SPM) methods presented here is a valuable key for the future
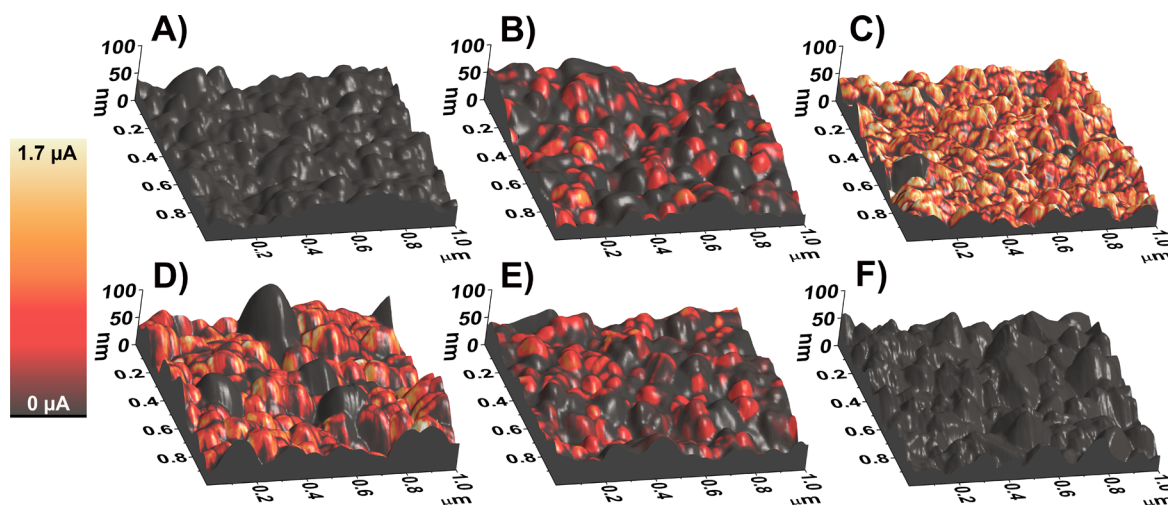
Figure 2. 3D topographical AFM images of LTO thin-films cycled to various states of charge. They correspond to (A) pristine, (B) discharged 50%, (C) discharged to 1.5 V, (D) discharged to 1.0 V, (E) charged 50%, and (F) charged to 2.0 V. The color scheme represents the current detected, as indicated by the scale bar at left.

optimization of this material, its composite electrode, and others like it.

RESULTS AND DISCUSSION

Thin-Film Bulk Characteristics. The common use of conductive additives in LTO composite electrodes can strongly influence the manner in which its electrochemical reaction occurs. This is evidenced by the great deal of research dedicated to creating LTO−carbon composites.[27−29] To determine how LTO's fundamental mechanism proceeds, therefore, we made use of thin-films that possessed only the electrochemically active material. LTO was grown on Pt-coated (*ca.* 225 nm) Al_2O_3 disks using RF magnetron sputtering and exhibited a thickness around 800 nm (Figure 1A). The Pt layer was incorporated to ensure good electrical contact for use in batteries as well as for c-AFM analysis; furthermore, it does not oxidize during the high temperature preparation anneal. Figure 1B illustrates the particle size distribution of deposited LTO, which was 20−100 nm on average. The film was highly crystalline, as demonstrated by the grazing incidence X-ray diffraction (GIXRD) in Figure 1C. Some LTO peaks show uncharacteristically high intensities, such as the (400) and (511) indices, due to overlapping contributions from Al_2O_3 substrate. A three-phase fit, incorporating all materials, was performed in order to confirm their structures and lattice parameters (Figure 1C, Table S1). LTO, Pt, and Al_2O_3 were fit to space groups $Fd\bar{3}m$, $Fm\bar{3}m$, and $R\bar{3}c$, respectively. The low residual, resulting in a conventional Rietveld factor (R_{wp}) of 7.18, confirms the purity of the film. The LTO lattice parameter was determined to be 8.3521 ± 0.0003, which is in excellent agreement with the values reported in literature.[30]

Figure 1D highlights the material's first electrochemical cycle and demonstrates very good reversibility over the first 10 cycles. The voltage response is the result of applying a constant current of 4 $\mu A \cdot cm^{-2}$ from 1.0 to 2.0 V upon charge/discharge. Given that the average reversible capacity upon cycling was around 30 $\mu Ah \cdot cm^{-2}$, the current corresponds to a rate of roughly C/7. The flat redox potential at 1.55 V *vs* Li/Li$^+$ is clearly indicative of the two-phase reaction between $Li_4Ti_5O_{12}$ and $Li_7Ti_5O_{12}$, as has been previously reported.[31,32] A nontrivial amount of capacity is shown to exist outside the voltage

window of 1.4 and 1.6 V during the first cycle, however, corresponding to 9.7 $\mu Ah \cdot cm^{-2}$ or roughly 20% of the initial discharge. Borghols *et al.* have demonstrated that this phenomenon occurs in LTO as its particle sizes decrease.[33] They hypothesize that a distribution of redox potentials are possible at the surface of LTO, due to unique structural environments there, which can result in local overlithiation. This behavior is also typical when cycling LTO thin-films and is likely due to the high fraction of LTO surface, relative to its bulk, in contact with electrolyte.[34] In addition, small side reactions occurring among cell components are commonly observed in thin-film electrochemistry due to the inherently low capacities resulting from the small amounts of active material. These surface effects are expanded upon in following sections of this paper.

The relatively large capacity outside of the plateau is not reversible, as highlighted in Figure S1. The capacity retention of the first cycle is about 60%, but immediately improves upon subsequent cycles, gradually increasing to near 95% by the 10th cycle. The amount of capacity outside of the 1.4−1.6 V window also decreases after the first cycle, to 4.3 $\mu Ah \cdot cm^{-2}$ (*ca.* 13%) during the second discharge. To explore the unique changes occurring in this system during the first cycle, we analyze the thin-films at the points indicated along the voltage profile in Figure 1D. The samples characterized specifically correspond to the following: (1) soaked pristine LTO, assembled into a cell, but not cycled; (2) LTO discharged to 50% of the initial discharge capacity; (3) LTO immediately following the voltage plateau, discharged to 1.5 V; (4) LTO fully discharged to 1.0 V; (5) LTO charged to 50% of the first charge capacity; (6) LTO fully charged to 2.0 V.

SPM Characterization. To establish whether mere exposure to electrolyte can affect the surface morphology of LTO, we allowed our pristine sample to equilibrate in an assembled battery for a day prior to c-AFM analysis. When we compare the 2D AFM height image in Figure S2a to the SEM image in Figure 1B, it is clear that no major structural changes occurred by simply soaking in electrolyte at open circuit. The average maximum height of features across multiple images of the pristine sample was 72.8 nm and it possessed a root-mean-square (RMS) surface roughness of 11.1 nm. Care was taken to
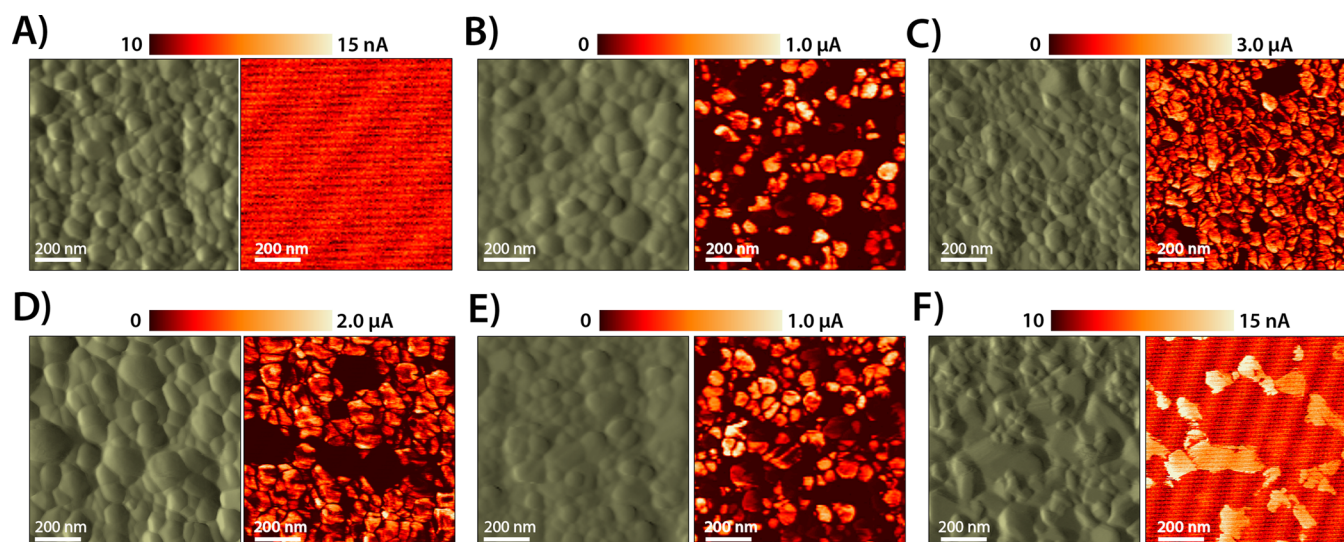
Figure 3. AFM deflection (left) and current (right) images of LTO thin-films cycled to various states of charge, corresponding to (A) pristine, (B) discharged 50%, (C) discharged to 1.5 V, (D) discharged to 1.0 V, (E) charged 50%, and (F) charged to 2.0 V. Note the difference in units between scale bars.

transfer and characterize LTO thin-films in an Ar atmosphere, as Kitta *et al.* have demonstrated that lithium-inserted samples can react with air to form precipitates on the surface.[35] Figure S2b shows that, upon discharging to 50% capacity, the surface morphology of lithiated LTO did not change appreciably. The average maximum height and surface roughness was 76.5 and 11.2 nm, respectively. A summary of surface dimensions for all samples is provided in Table S2.

While the morphology did not change upon initial discharge, due to negligible volume expansion upon lithiation, the electronic conductivity measured using c-AFM significantly increased. Figure 2 depicts the current response of all samples when a potential of 0.4 V was applied between the c-AFM tip and substrate. While no current is observed in the pristine material, it is measured within an array of individual grains upon discharging to 50% capacity. The average current measured in the latter sample was 0.12 $\mu A\cdot\mu m^{-2}$. After discharging just past the plateau, to 1.5 V (Figure 2C), the magnitude and distribution of current increased from 0.12 to 0.58 $\mu A\cdot\mu m^{-2}$. The total current measured in each sample is represented by the histograms shown in Figure S3. Figure 2C demonstrates that, immediately following the total lithiation, or completion of the two-phase reaction, nearly all grains in the LTO film are electronically conductive.

Kim *et al.* hypothesized that within LTO possessing no conductive additive, a conductive $Li_7Ti_5O_{12}$ phase first forms in the vicinity of immediate contact with the current collector.[23] Upon further discharge, this phase was thought to evenly propagate upward, through all particles, toward the interface with electrolyte. The deflection and current images provided in Figure 3, however, show that this is not the case for these thin-film electrodes. In the sample discharged 50% (Figure 3B), we clearly observe current localized within discrete grains, not evenly across the surface. This suggests that the transition of $Li_4Ti_5O_{12}$ to $Li_7Ti_5O_{12}$ proceeds *via* a limited number of narrow percolation channels that connect current collector and electrolyte. Figure S4 qualitatively illustrates the difference. There are a number of regions with near-identical grains adjacent to one another, which exhibit current in one and not the other. Furthermore, the particles themselves are very well-defined in the current images of Figure 3C. This is because no current is measured within grain boundaries, suggesting the phase transition does not propagate laterally across grains. This may be due to unique structural environments that connect these grain interfaces.

When discharge occurred beyond 1.5 V to the typical LTO cutoff voltage of 1.0 V, the average particle size significantly increased, resulting in an RMS surface roughness of 16.4 nm. In addition, the measured current decreased somewhat, to 0.32 $\mu A\cdot\mu m^{-2}$. Figures 2D and 3D demonstrate that all grains exhibit lower electronic conductivity overall, but very large grains show none. One factor contributing to these changes may be due to the formation of solid−electrolyte interface (SEI) products. Although LTO is not commonly believed to form a SEI, due to its high operating voltage, the high surface area of thin-films enhances the reactions occurring there, relative to its bulk. Another contributing factor may be due to the local overlithiation of LTO at its surface. These hypotheses are more fully described in a following section, where we analyze these samples using XPS.

The change in surface morphology is not completely irreversible, as subsequently charging to 50% capacity results in reduced grain sizes, with an intermediate RMS surface roughness of 13.5 nm. Furthermore, the RMS surface roughness of LTO charged completely to 2.0 V nearly reaches its original value, at 12.1 nm. Though grain sizes decrease on average, the AFM deflection image in Figure 3F shows the formation of a different grain morphology, which is composed of a large proportion of well-defined flattened regions. In addition, Figure 3F shows that the relatively large flat regions are slightly conductive. The fact that some current exists in the fully charged state suggests that a semipermanent conductive percolation network may form upon the initial charge, thus reducing the activation potential required for subsequent cycles. Indeed, the electrochemical efficiency is shown to improve upon cycling; an embedded conductive matrix that increases over time may be partially responsible for this.

To summarize and compare the wide range of measured currents (from nA to μA), the log(current) values of all samples are shown in Figure 4. Current histograms of the measured c-
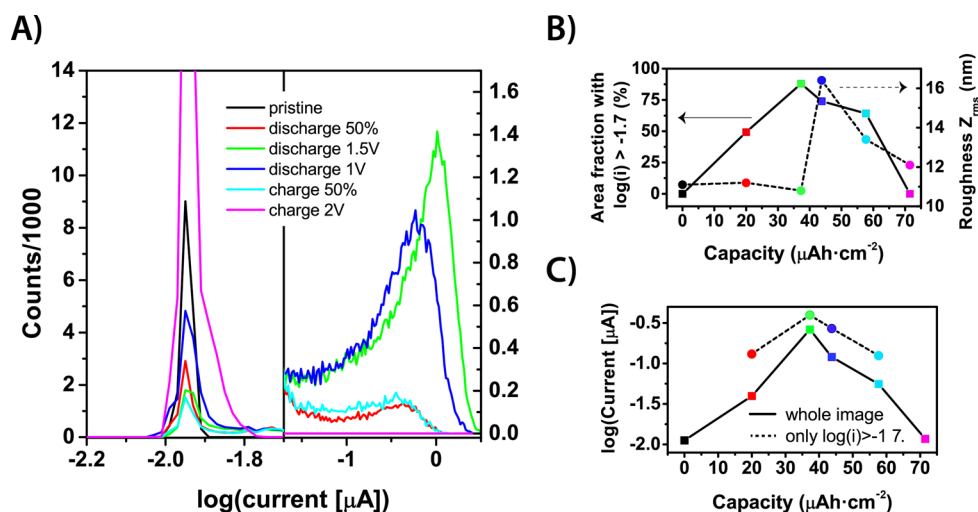
Figure 4. (A) Histograms of c-AFM images for all samples divided in two regimes. (B) Area fraction of regions where current is measured (left axis), as well as surface roughness (right axis), as a function of the first cycle capacity. Note that discharge to 1.5 V and 1.0 V corresponds to 37 $\mu A \cdot cm^2$ and 44 $\mu A \cdot cm^2$, respectively. Larger capacities correspond to the first charge. (C) Average current measured in whole images of Figure 3 and average current measured in areas exhibiting current above a certain threshold.
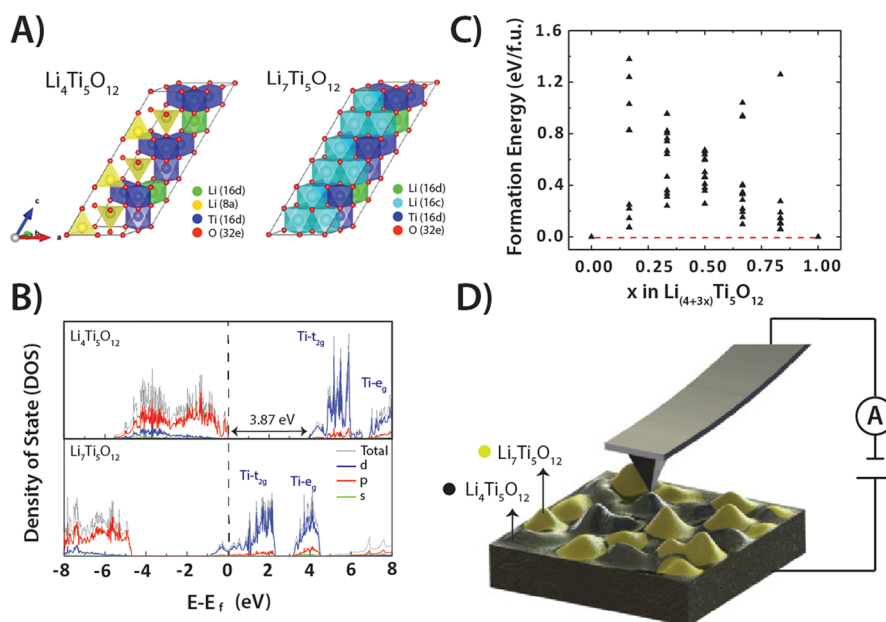

Figure 5. (A) Structurally optimized $Li_4Ti_5O_{12}$ and $Li_7Ti_5O_{12}$ lattices. (B) Density of state (DOS) calculations for $Li_4Ti_5O_{12}$ and $Li_7Ti_5O_{12}$, where the Fermi energy is normalized to 0 eV. (C) Formation energy of possible intermediate phases of various Li concentrations, with respect to $Li_4Ti_5O_{12}$ and $Li_7Ti_5O_{12}$ end members. (D) Illustration of c-AFM capability to detect the presence of each phase due to their unique conductivities.

AFM images are depicted in Figure 4A. On the left is the low current region, with the single peak corresponding to noise at the instrument's detection limit. On the right is the high current region, resulting from current measured because of changes among each sample. As the LTO sample is discharged, its measured current increases, which results in the low current peak decreasing and the high current peak increasing, until it reaches its maximum when discharged to 1.5 V. Further discharge to 1.0 V reduces the current and the area fraction of regions showing current, with a strong increase in surface roughness (Figure 4B,C). Upon charge, the average current and surface roughness decrease again. While the average current of samples discharged and charged to 50% were fairly similar, their RMS surface roughnesses were not. The difference in

morphology is likely related to the first cycle partial irreversibility, where surface reconstruction occurred below 1.5 V of the initial discharge.

LTO Lithiation and Electronic Properties. We applied DFT to describe the phases contributing to the local electronic conductivity of each sample with more certainty. To calculate the density of states (DOS) for $Li_4Ti_5O_{12}$ (LTO) and $Li_7Ti_5O_{12}$ (lithiated LTO), we built their model systems and performed structural optimization calculations. Those structures are shown in Figure 5A. We adopted $2Li_4Ti_5O_{12}$ since it has the smallest number of atoms representing LTO. The structure belongs to the $Fd\bar{3}m$ space group and consists of both Li in 8a sites and Li or Ti in 16d sites. Oxygen in 32e sites are tetrahedrally coordinated to 8a sites and octahedrally coordinated to 16d
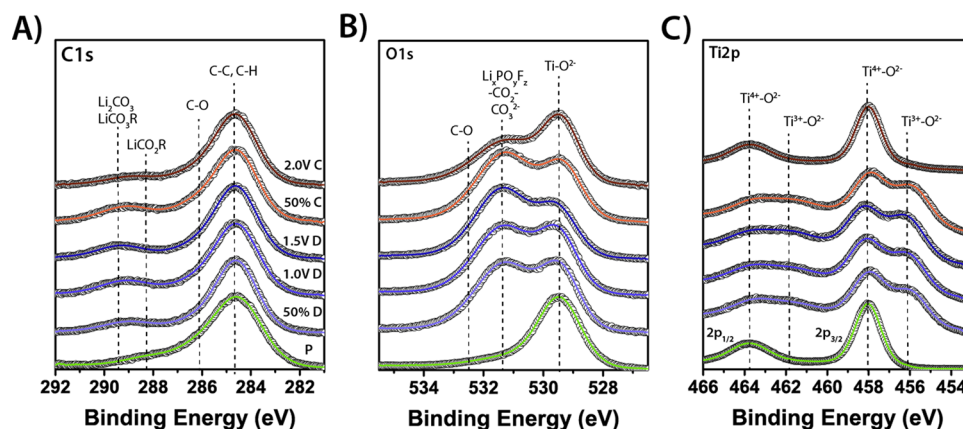
Figure 6. Normalized high-resolution C 1s (A), O 1s (B), and Ti 2p (C) XPS spectra of the LTO thin-films discharged (blue) and then charged (red). From bottom to top is pristine (P), discharged 50% (50% D), discharged to 1.5 V (1.5 V D), discharged to 1.0 V (1.0 V D), charged 50% (50% C), and charged to 2.0 V (2.0 V C).
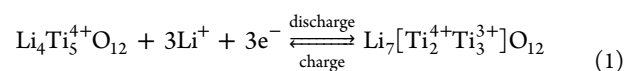
sites. Furthermore, one Li for every five Ti ions are occupied in 16d sites. It was determined that the lowest energy LTO structure occurred when octahedrally coordinated Li ions were located furthest away from one another, which is shown by the green Li in Figure 5A. Upon lithiation, the original Li ions in 8a sites (yellow), together with intercalated Li ions, migrate to 16c sites (cyan) to form $Li_7Ti_5O_{12}$. We confirmed the lattice parameter of fully relaxed LTO and its lithiated form, which were calculated using the PBE functional. The values were determined to be 8.44 and 8.38 Å, respectively, which corresponds to experimentally reported values reasonably well, with an error of less than 0.95%.[36]

A range of experimentally determined band gaps have been reported for LTO. Those values are commonly determined to be between 3.0 and 4.0 eV, with the most typical reported being *ca.* 3.8 eV.[12,23,37] Standard DFT calculations, however, underestimate the band gap to be between 1.7 and 2.3 eV, as the GGA functional is not able to properly describe the electron–electron correlation–exchange interaction.[38−40] To measure a more accurate band gap, we adopted the HSE06 hybrid functional into our LTO calculations. This functional is capable of improving the band gap calculation by subtle tuning of the weight of the Hartree–Fock exchange toward the GGA exchange and correlation. We also confirmed the dependence of LTO's band gap on the Hartree–Fock mixing contribution, which is shown in Figure S5. The results indicate that the band gap is linearly dependent on the percent contribution of the exact Hartree–Fock exchange. We found that a hybrid functional contribution of 30% exhibits a band gap of 3.87 eV, which is most compatible with experimentally determined band gaps.

Figure 5B shows the electronic structure of LTO within the hybrid functional framework described above. The DOS demonstrates the band gap of 3.87 eV, which is primarily defined by the O 2p and Ti 3d bands. Interestingly, we confirmed the breaking of degeneracies of Ti 3d orbitals into t_{2g} and e_g energy levels. This is a common phenomenon, which originates from the octahedral crystal field. Electrons in pristine LTO do not occupy t_{2g} and e_g levels because the oxidation state of all Ti ions is 4+, in which Ti 3d electrons do not exist. We again applied the 30% Hartree–Fock mixing parameter on lithiated LTO, which is shown in Figure 5B. Upon lithiation, Li ions as well as electrons are incorporated into LTO, resulting in $Li_7Ti_5O_{12}$. This phase has three Ti^{3+} and two Ti^{4+} so that the

lower energy t_{2g} level is partially filled. The DOS of $Li_7Ti_5O_{12}$ is continuous across the Fermi level, which demonstrates that the lithiated phase is an electronic conductor.

To further determine how LTO lithiation/delithiation proceeds, we set up 68 possible intermediate phases and performed DFT calculations using the PBE functional (Figure 5C). We modeled intermediate phases by allocating or removing Li ions into 16c sites of the LTO or lithiated LTO phases shown in Figure 5A. The results indicate that the formation of intermediate phases is unfavorable. The formation energies of the possible $Li_{4+3x}Ti_5O_{12}$ $(0 < x < 1)$ intermediate phases are all positive (the system favors a composite mixture of $Li_4Ti_5O_{12}$ and $Li_7Ti_5O_{12}$) in Figure 5C, which shows that there is no intermediate phase more energetically stable than a mixture of the end phases. The formation of the thermodynamically most stable end members supports the hypothesis that lithiation/delithiation occurs by means of a two-phase reaction and not *via* a solid solution mechanism. This reaction is described by the following equation, whereby 3 Ti^{4+} per formula unit are reduced to Ti^{3+}:

$$Li_4Ti_5^{4+}O_{12} + 3Li^+ + 3e^- \underset{charge}{\overset{discharge}{\rightleftharpoons}} Li_7[Ti_2^{4+}Ti_3^{3+}]O_{12} \quad (1)$$

Wagemaker *et al.* claim that the two-phase reaction is kinetically induced, but relaxes to a solid solution at equilibrium.[36] Our results suggest that even at equilibrium, however, the formation of an intermediate phase is not favorable. This discrepancy might be caused by the difference between using a model LTO system and a composite electrode. Any conductive species to be observed in our case would specifically be $Li_7Ti_5O_{12}$ and not $Li_{4+3x}Ti_5O_{12}$, $0 < x < 1$. By performing c-AFM on partially lithiated samples, we therefore observe discrete domains of $Li_4Ti_5O_{12}$ and $Li_7Ti_5O_{12}$, as conceptually illustrated in Figure 5D.

LTO Surface Chemistry. To further understand the LTO phase transition and the evolution of surface chemistry during the first cycle, we performed XPS on thin-films cycled to the same states of charge described previously. Figure 6 shows high-resolution scans of the C 1s, O 1s, and Ti 2p regions. The single peak centered at 458.0 eV corresponds very well to the $2p_{3/2}$ peak of Ti^{4+} in LTO, as well as in TiO_2.[41,42] Upon discharge, a second peak at 455.9 eV forms, which corresponds to Ti^{3+} measured in Ti_2O_3.[43] This peak reaches a maximum relative to the Ti^{4+} peak, in the LTO sample discharged to 1.0 V
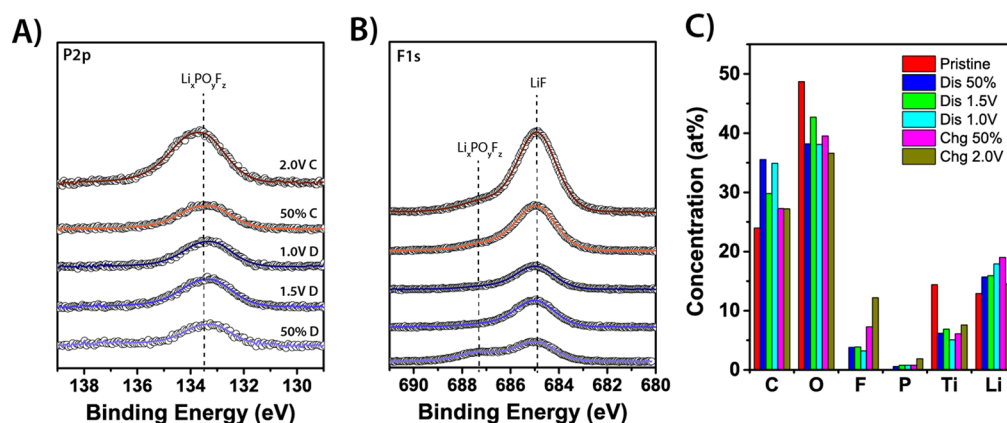
Figure 7. Non-normalized high-resolution (A) P 2p and (B) F 1s XPS spectra of LTO thin-films discharged (blue) and then charged (red). From bottom to top is discharged 50% (50% D), discharged to 1.5 V (1.5 V D), discharged to 1.0 V (1.0 V D), charged 50% (50% C), and charged to 2.0 V (2.0 V C). (C) Elemental surface compositions of LTO obtained from XPS survey scans. Note that the increase in P and F concentrations are related to a decrease in the content of the organics species as electrochemical charging occurs.

and correlates to the formation of Ti^{3+} due to reduction of Ti^{4+} upon lithiation. The relative intensity of the Ti^{3+} peak decreases upon charge and completely disappears at 2.0 V, indicating that the surface reaction is fully reversible. This evolution is further observed in the Ti 3s data shown in Figure S6. It is interesting to note that the proportion of Ti^{3+} measured at 50% state of discharge is higher than expected from the reduction of 1.5 of the 5 Ti^{4+}, to Ti^{3+} (eq 1). For example, the increase in Ti^{3+} content from 50% state of discharge to 1.0 V does not double to account for the conversion of an additional 1.5 Ti^{4+} into 1.5 Ti^{3+}. This result suggests that a higher concentration than 1.5 Ti^{3+} per 5 Ti formula units has formed on the surface during the first 50% of the discharge. Moreover, as suggested above, this result further supports that the transformation of Ti^{4+} ($Li_4Ti_5O_{12}$) into Ti^{3+} ($Li_7Ti_5O_{12}$) is not a spatially homogeneous process extending from the current collector interface to the surface in contact with the electrolyte.

The peak in the O 1s spectra at 529.7 eV corresponds to O^{2-} in the LTO lattice.[44] Upon discharge, a peak at 531.5 eV grows relative to it, and reaches a maximum at 1.0 V. This higher binding energy peak results from the contributions of several solid electrolyte interface (SEI) species, including CO_3^{2-}, $-CO_2-$, and $Li_xPO_xF_z$, all of which originate from the decomposition of electrolyte.[45] The formation of decomposition products, Li_2CO_3 and/or $LiCO_3R$, are also shown to significantly occur in the sample discharged to 1.0 V, as suggested by the signal in the C 1s peak near 289.5 eV.[46] The fact that we observe these species is significant because LTO is excessively championed to form no passivation or SEI layers, due to its high redox potential. This is clearly not the case. Indeed, LTO is known to have major gassing issues, which result from its interaction with alkyl carbonated-based solvents.[47] He *et al.* have also reported that LTO with very high surface areas can exhibit SEI.[48] The nature of working with thin-films is such that a significant amount of the active mass is in direct contact with electrolyte. Any reaction with electrolyte can be amplified, therefore, as the material's surface to volume ratio, and hence the thin-film/electrolyte interface, is relatively large compared to powder electrodes. The formation of these electrolyte decomposition products may be partially responsible for the material's extended first cycle discharge capacity. A passivation layer may form upon initial discharge (below 1.5 V) to create a relatively stable SEI; since subsequent cycles show

markedly improved capacity retention, this reduction of electrolyte would not appear to occur continuously.

Figure 7 shows that the peaks in the P 2p and F 1s spectra, corresponding to $Li_xPO_yF_z$ at 133.7 eV and LiF at 685.1 eV, both increase significantly upon charge. Figure 7 also depicts the elemental compositions derived from the XPS survey scans. This plot shows that the degree of F and P increase significantly upon charge, from 7.3 to 12.2% (F) and 0.8 to 1.9% (P) in samples charged to 50% and 2.0 V, respectively. The full percent abundance of all species derived from component fitting of the high-resolution scans is provided in Table S3. As it can be seen, the increase in F and P concentrations is correlated with a decrease in the organic species concentrations discussed above, as well as with an increase of the Ti 2p and O 1s lattice signals. Hence, both results support the removal of part of the organic species generally present in the top part of the SEI film. Moreover, the stronger F and P signals are likely due to a shorter escape depth for the photoelectrons coming from the inorganic part of the SEI layer since less organic material is present on top of it.

Figure 6B and Table S3 show that lattice oxygen is least abundant at the surface of LTO discharged to 1.0 V. The SEI formed at that point may partly contribute to the increased grain sizes observed using AFM. Kitta *et al.* also observed changes in LTO morphology upon lithium insertion, which they attributed to phase changes occurring at the surface.[35] In addition, Ganapathy *et al.* performed computational studies that showed the electrochemical overlithiation of $Li_7Ti_5O_{12}$ was possible at the surface of LTO due to preferred orientation and relaxation effects occurring at this interface.[49] Wang *et al.* further supported this hypothesis by analyzing deeply discharged LTO samples using TEM-EELS.[50] They propose the additional insertion of Li into vacant 8a sites would cause structural distortions due to the large Coulomb repulsions. Because the surface to volume ratio of our thin-film samples is inherently high, the extra capacity, lower Ti valence states, and surface reconstruction observed when discharging beyond 1.5–1.0 V may likely be the result of overlithiation. Where the extent of overlithiation occurs most may lead to either delamination of grains from the current collector or the formation of nonconductive species, as larger volume particles clearly show no conductivity. Figure 6C shows that the abundance of Li at the surface of LTO increases from 1.5 to 1.0

V. High-resolution spectra of the Li 1s regions are provided in Figure S6 and show evidence of Li^+ in the LTO lattice, organic and inorganic SEI species (LiF, *etc.*). Further work would be necessary to accurately monitor the evolution of the Li^+ signal from the LTO lattice using, for instance, angle resolved synchrotron XPS, to confirm and discuss the existence of LTO surface overlithiation.

CONCLUSIONS

This work directly visualizes the two-phase transformation between $Li_4Ti_5O_{12}$ and $Li_7Ti_5O_{12}$ at the nanoscale. By cycling LTO to various states of charge and measuring the local current in response to a fixed potential bias, we were able to determine exactly where each phase existed at those states of charge. As opposed to prevailing theories, we determined that the transition of $Li_4Ti_5O_{12}$ to $Li_7Ti_5O_{12}$ proceeds *via* percolation channels within single grains. The reaction does not appear to propagate laterally, across grain boundaries. It also does not form evenly throughout the electrode from one interface to the other. Upon discharge beyond the 1.55 V redox plateau, to 1.0 V, significant changes in surface morphology and conductivity occurred. Using XPS, we demonstrated that this was related to the reaction between LTO and electrolyte, and likely, from LTO overlithiation, from 1.5 to 1.0 V. The combination of c-AFM and XPS described provides a more detailed understanding of the LTO lithiation/delithiation process. These insights may be used to optimize other electrode materials with insulator to metal transitions behaviors.

MATERIALS AND METHODS

Synthesis. $Li_4Ti_5O_{12}$ powder for sputter target preparation was synthesized by ball milling stoichiometric amounts of Li_2CO_3 (Mallinckrodt −99.5+%) and TiO_2 (Aldrich, Anatase 99.9+%, which was pressed into a 2 in. diameter disk and then fired in air at 950 °C for 10 h. To ensure O_2 recovery upon cooling, the disk was cooled slowly at 0.5 °C·min^{-1} to 700 °C, which was held for 20 h, and finally cooled down at 10 °C·min^{-1} to room temperature. The dense pellet was subsequently bound to a Cu plate and used as a target for magnetron sputtering. LTO films were grown by means of r.f. magnetron sputtering in an Ar atmosphere (Air Liquide, Research grade, 99.99995%), at an applied RF power of 80 W, at a pressure of 5 mTorr, where deposition was performed once the base pressure in the chamber reached at least 10^{-6} Torr. The films were grown on 1 cm Al_2O_3 disks (Valley Design) coated with 0.25 μm of Pt (Refining Systems, Las Vegas, NV, 99.99%) on both sides, which acted as the negative electrode current collector. Sputtering of the Pt was performed in direct current mode using 25 W and 15 mTorr Ar pressure. The as-deposited LTO films, with a typical thickness of 800 nm, were annealed in air at 700 °C for 1 h to develop the spinel structure.

Electrochemical Cells. LTO thin-films were assembled into standard Swagelok cells, in an Ar-filled glovebox. Li foil (0.75 mm Alfa Aesar, 99.99%) was used as anode, two-sheets of Celgard 2500 served as separator, and the electrolyte was composed of 1.2 M $LiPF_6$ in ethylene carbonate/ethyl methyl carbonate (Novolyte). A Maccor Battery Tester was used to galvanostatically cycle cells at a current of 4 μA·cm^{-2}, between 1.0 and 2.0 V. Cells used for further analysis were stopped at various points during the first cycle and are described by the following: (1) LTO prior to cycling (pristine or P); (2) LTO discharged to 50% of the initial discharge capacity (50% D); (3) LTO discharged to 1.5 V into the initial discharge (1.5 V D); (4) LTO discharged to 1.0 V into the initial discharge (1.0 V D); (5) LTO charged to 50% of the initial charge capacity, following discharge to 1.0 V (50% C); (6) LTO charged to 2.0 V into the initial charge, following discharge to 1.0 V (2.0 V C). The voltage profiles of these samples are shown in Figure S1. The pristine sample used before cycling was

assembled into a Swagelok cell and allowed to equilibrate in electrolyte for 24 h before disassembly. All other cells were disassembled immediately following their electrochemical exit condition to prevent additional chemical reaction with electrolyte. Following disassembly in a glovebox, LTO thin-films were rinsed with anhydrous dimethyl carbonate (Aldrich, 99% anhydrous) to remove residual electrolyte. They were left to dry within the glovebox before transporting within a sealed, airtight, Ar-filled container.

GIXRD and SEM. The focused ion beam (FIB) cross section of LTO was fabricated with an FEI Scios, using a 1.0 nA Ga^+ beam current, at 30 kV. The scanning electron microscopy (SEM) image was acquired using a 0.1 nA current, at 5 kV. Grazing incidence X-ray diffraction (GIXRD) was collected using a Rigaku SmartLab X-ray diffractometer, utilizing the Parallel Beam/Parallel Slit Analyzer mode. The incident angle was 0.5° and the incident slit was 0.5 mm. The data was collected from 15 to 80° 2θ, with a 0.05° step at 1°·min^{-1}.

SPM. Atomic force microscopy (AFM) was performed using an Asylum Research Cypher S, housed within an Ar-filled glovebox. Pt-coated tips (Nanosensors) with a radius of curvature of 20−50 nm at the apex were used for conductivity (c-AFM) measurements. LTO thin-films were transported in sealed Ar-filled transfer chambers between glove boxes and were never exposed to air. Inside the glovebox the thin-films were mounted onto two-sided Cu-clad circuit board using silver paste. The paste was applied to Pt on the sample backside, as well as a portion of the side and top of the thin-film, which ensured electrical contact throughout the entire film. These mounted thin-films are shown in Figure S7. This figure also demonstrates the port connecting the circuit board and thin-film to the AFM tip. A fixed voltage of 0.4 V was applied between the tip and sample during scans. The current was measured using a 10^6 V·A^{-1} amplifier gain. Height and deflection images were processed using the flattening feature of WSxM software (5.0 Develop 4.3).[51]

Computation. The Generalized Gradient Approximation (GGA) by Perdew−Burke−Ernzerhof (PBE), as implemented in the Vienna *Ab initio* Simulation Package (VASP), was adopted to describe the exchange-correlation energies of electrons in LTO.[52−54] The interaction potentials of the core electrons were replaced by Projector Augmented Wave (PAW) pseudopotentials.[55] In all calculations, Li ($1s^2 2s^1$), Ti ($3p^6 3d^3 4s^1$), and O ($2s^2 2p^4$) are treated as the valence electron configurations. A gamma point mesh with $6 \times 6 \times 2$ k-points was specified in the Brillouin zone, and periodic boundary conditions were imposed on our calculations. The plane-wave energy cutoff was set to 520 eV, which is 1.3 times the maximum cutoff specified by the pseudopotential of oxygen in the VASP. We set the electronic energy difference required for convergence to 10^{-4} eV. All the atoms were fully relaxed to simulate the optimized structure of each lattice model. The density of states (DOS) for structurally optimized $Li_4Ti_5O_{12}$ and $Li_7Ti_5O_{12}$ were calculated using the tetrahedron method with Blöchl corrections.[56] We used the Heyd−Scuseria−Ernzerhof (HSE06) hybrid functional to produce the exact band gaps of $Li_4Ti_5O_{12}$ and $Li_7Ti_5O_{12}$.[57,58] We also tuned 30% of the exact Hartree−Fock (HF) exchange contribution to the hybrid functional in order to bench-mark the experimental band gap of $Li_4Ti_5O_{12}$.

XPS. A PHI 3056 spectrometer possessing a concentric hemispherical analyzer 54.7° off normal and a dual Mg and Al anode source, operating at 15 kV and 350 W, was used for all XPS analyses. LTO thin-films were transferred from an Ar-filled glovebox *via* a custom airtight chamber for direct transfer to the spectrometer, without exposure to air. The XPS chamber was maintained at $<10^{-8}$ Torr during measurement. High-resolution scans made use of the Al source (1486.7 eV), using a pass energy of 23.5 eV and a step size of either 0.05 or 0.075 eV. Each scan was preceded by a high-resolution C 1s scan, to account for charge buildup. XPS processing was performed using CasaXPS software. The main C 1s peak was calibrated to carbon black, 284.6 eV, as were the following high-resolution scans. Peaks were decomposed using Gaussian−Lorentzian line shapes and Shirley background subtractions.

ASSOCIATED CONTENT

ⓢ Supporting Information

The Supporting Information is available free of charge on the ACS Publications website at DOI: 10.1021/acsnano.5b07875.

Tables detailing thin-film refinement parameters, currents, surface roughnesses, and chemistries are included; additional figures demonstrating computational details, electrochemical retention, experimental c-AFM design for thin-films, their height and line profiles, current distributions, 3D topographies, an illustration to describing the phase transformation, and additional XPS spectra (PDF)

AUTHOR INFORMATION

Corresponding Authors

*E-mail (M.G.V) mverdejr@gmail.com.
*E-mail (Y.S.M) shmeng@ucsd.edu.

Present Address

⊥Centre Interuniversitaire de Recherche et d'Ingéniérie des Matériaux (CIRIMAT), UMR5085 CNRS, 4 allée Emile Monso, BP-44362, 31030 Toulouse Cedex 4, France.

Notes

The authors declare no competing financial interest.

ACKNOWLEDGMENTS

REFERENCES

(1) Park, C.-M.; Kim, J.-H.; Kim, H.; Sohn, H.-J. Li-alloy Based Anode Materials for Li Secondary Batteries. *Chem. Soc. Rev.* **2010**, *39*, 3115−3141.

(2) Zhu, G. N.; Wang, Y. G.; Xia, Y. Y. Ti-Based Compounds as Anode Materials for Li-ion Batteries. *Energy Environ. Sci.* **2012**, *5*, 6652−6667.

(3) Goodenough, J. B.; Kim, Y. Challenges for Rechargeable Li Batteries. *Chem. Mater.* **2010**, *22*, 587−603.

(4) Oumellal, Y.; Delpuech, N.; Mazouzi, D.; Dupre, N.; Gaubicher, J.; Moreau, P.; Soudan, P.; Lestriez, B.; Guyomard, D. The Failure Mechanism of Nano-Sized Si-Based Negative Electrodes for Lithium ion Batteries. *J. Mater. Chem.* **2011**, *21*, 6201−6208.

(5) Ohzuku, T.; Ueda, A.; Yamamoto, N. Zero-Strain Insertion Material of Li[Li$_{1/3}$Ti$_{5/3}$]O$_4$ for Rechargeable Lithium Cells. *J. Electrochem. Soc.* **1995**, *142*, 1431−1435.

(6) Aravindan, V.; Lee, Y.-S.; Madhavi, S. Research Progress on Negative Electrodes for Practical Li-Ion Batteries: Beyond Carbonaceous Anodes. *Adv. Energy Mater.* **2015**, *5*, 1402225.

(7) Takami, N.; Hoshina, K.; Inagaki, H. Lithium Diffusion in Li$_{4/3}$Ti$_{5/3}$O$_4$ Particles During Insertion and Extraction. *J. Electrochem. Soc.* **2011**, *158*, A725−A730.

(8) Chen, C. H.; Vaughey, J. T.; Jansen, A. N.; Dees, D. W.; Kahaian, A. J.; Goacher, T.; Thackeray, M. M. Studies of Mg-Substituted Li$_{4-x}$Mg$_x$Ti$_5$O$_{12}$ Spinel Electrodes ($0 \leq x \leq 1$) for Lithium Batteries. *J. Electrochem. Soc.* **2001**, *148*, A102−A104.

(9) Nitta, N.; Yushin, G. High-Capacity Anode Materials for Lithium-Ion Batteries: Choice of Elements and Structures for Active Particles. *Particle & Particle Systems Characterization* **2014**, *31*, 317−336.

(10) Rho, Y. H.; Kanamura, K. Li$^+$ Ion Diffusion in Li$_4$Ti$_5$O$_{12}$ Thin Film Electrode Prepared by PVP Sol-Gel Method. *J. Solid State Chem.* **2004**, *177*, 2094−2100.

(11) Edwards, P. P.; Egdell, R. G.; Fragala, I.; Goodenough, J. B.; Harrison, M. R.; Orchard, A. F.; Scott, E. G. A Study of the Spinel Materials LiTi$_2$O$_4$ and Li$_{4/3}$Ti$_{5/3}$O$_4$ by Photoelectron Spectroscopy. *J. Solid State Chem.* **1984**, *54*, 127−135.

(12) Kostlánová, T.; Dedecek, J.; Krtil, P. The Effect of the Inner Particle Structure on the Electronic Structure of the Nano-Crystalline Li-Ti-O Spinels. *Electrochim. Acta* **2007**, *52*, 1847−1856.

(13) Luo, H.; Shen, L.; Rui, K.; Li, H.; Zhang, X. Carbon coated Li$_4$Ti$_5$O$_{12}$ Nanorods as Superior Anode Material for High Rate Lithium Ion Batteries. *J. Alloys Compd.* **2013**, *572*, 37−42.

(14) Zhang, Q.; Verde, M. G.; Seo, J. K.; Li, X.; Meng, Y. S. Structural and Electrochemical Properties of Gd-Doped Li$_4$Ti$_5$O$_{12}$ as Anode Material with Improved Rate Capability for Lithium-Ion Batteries. *J. Power Sources* **2015**, *280*, 355−362.

(15) Zhang, Q.; Zhang, C.; Li, B.; Jiang, D.; Kang, S.; Li, X.; Wang, Y. Preparation and Characterization of W-doped Li$_4$Ti$_5$O$_{12}$ Anode Material for Enhancing the High Rate Performance. *Electrochim. Acta* **2013**, *107*, 139−146.

(16) Zhang, Q.; Zhang, C.; Li, B.; Kang, S.; Li, X.; Wang, Y. Preparation and Electrochemical Properties of Ca-Doped Li$_4$Ti$_5$O$_{12}$ as Anode Materials in Lithium-Ion Battery. *Electrochim. Acta* **2013**, *98*, 146−152.

(17) Chen, S.; Xin, Y.; Zhou, Y.; Ma, Y.; Zhou, H.; Qi, L. Self-Supported Li$_4$Ti$_5$O$_{12}$ nanosheet Arrays for Lithium Ion Batteries with Excellent Rate Capability and Ultralong Cycle Life. *Energy Environ. Sci.* **2014**, *7*, 1924−1930.

(18) Wagemaker, M.; Mulder, F. M.; Van der Ven, A. The Role of Surface and Interface Energy on Phase Stability of Nanosized Insertion Compounds. *Adv. Mater.* **2009**, *21*, 2703−2709.

(19) Liu, J.; Song, K.; van Aken, P. A.; Maier, J.; Yu, Y. Self-Supported Li$_4$Ti$_5$O$_{12}$-C Nanotube Arrays as High-Rate and Long-Life Anode Materials for Flexible Li-Ion Batteries. *Nano Lett.* **2014**, *14*, 2597−2603.

(20) Li, N.; Zhou, G.; Li, F.; Wen, L.; Cheng, H.-M. A Self-Standing and Flexible Electrode of Li$_4$Ti$_5$O$_{12}$ Nanosheets with a N-Doped Carbon Coating for High Rate Lithium Ion Batteries. *Adv. Funct. Mater.* **2013**, *23*, 5429−5435.

(21) Tang, Y.; Zhang, Y.; Li, W.; Ma, B.; Chen, X. Rational Material Design for Ultrafast Rechargeable Lithium-ion Batteries. *Chem. Soc. Rev.* **2015**, *44*, 5926−5940.

(22) Song, M.-S.; Benayad, A.; Choi, Y.-M.; Park, K.-S. Does Li$_4$Ti$_5$O$_{12}$ Need Carbon in Lithium Ion Batteries? Carbon-Free Electrode with Exceptionally High Electrode Capacity. *Chem. Commun. (Cambridge, U. K.)* **2012**, *48*, 516−518.

(23) Kim, C.; Norberg, N. S.; Alexander, C. T.; Kostecki, R.; Cabana, J. Mechanism of Phase Propagation During Lithiation in Carbon-Free Li$_4$Ti$_5$O$_{12}$ Battery Electrodes. *Adv. Funct. Mater.* **2013**, *23*, 1214−1222.

(24) Young, D.; Ransil, A.; Amin, R.; Li, Z.; Chiang, Y.-M. Electronic Conductivity in the Li$_{4/3}$Ti$_{5/3}$O$_4$−Li$_{7/3}$Ti$_{5/3}$O$_4$ System and Variation with State-of-Charge as a Li Battery Anode. *Adv. Energy Mater.* **2013**, *3*, 1125−1129.

(25) Scharner, S.; Weppner, W.; Schmid-Beurmann, P. Evidence of Two-Phase Formation Upon Lithium Insertion into the Li$_{1.33}$Ti$_{1.67}$O$_4$ spinel. *J. Electrochem. Soc.* **1999**, *146*, 857−861.

(26) Kanamura, K.; Umegaki, T.; Naito, H.; Takehara, Z.; Yao, T. Structural and Electrochemical Characteristics of Li$_{4/3}$Ti$_{5/3}$O$_4$ as an Anode Material for Rechargeable Lithium Batteries. *J. Appl. Electrochem.* **2001**, *31*, 73−78.

(27) Guo, X.; Wang, C.; Chen, M.; Wang, J.; Zheng, J. Carbon Coating of $Li_4Ti_5O_{12}$ Using Amphiphilic Carbonaceous Material for Improvement of Lithium-Ion Battery Performance. *J. Power Sources* **2012**, *214*, 107−112.

(28) Ding, Z.; Zhao, L.; Suo, L.; Jiao, Y.; Meng, S.; Hu, Y.-S.; Wang, Z.; Chen, L. Towards Understanding the Effects of Carbon and Nitrogen-Doped Carbon Coating on the Eectrochemical performance of $Li_4Ti_5O_{12}$ in Lithium Ion Batteries: A Combined Experimental and Theoretical Study. *Phys. Chem. Chem. Phys.* **2011**, *13*, 15127−15133.

(29) Zhang, B.; Huang, Z.-D.; Oh, S. W.; Kim, J.-K. Improved Rate Capability of Carbon Coated $Li_{3.9}Sn_{0.1}Ti_5O_{12}$ Porous Electrodes for Li-ion Batteries. *J. Power Sources* **2011**, *196*, 10692−10697.

(30) Nakayama, M.; Ishida, Y.; Ikuta, H.; Wakihara, M. Mixed Conduction for the Spinel Type $(1-x)Li_{4/3}Ti_{5/3}O_4·LiCrTiO_4$ System. *Solid State Ionics* **1999**, *117*, 265−271.

(31) Li, D.; Zhou, H. Two-Phase Transition of Li-Intercalation Compounds in Li-ion Batteries. *Mater. Today* **2014**, *17*, 451−463.

(32) Kitta, M.; Akita, T.; Tanaka, S.; Kohyama, M. Characterization of Two Phase Distribution in Electrochemically-Lithiated Spinel $Li_4Ti_5O_{12}$ Secondary Particles by Electron Energy-Loss Spectroscopy. *J. Power Sources* **2013**, *237*, 26−32.

(33) Borghols, W. J. H.; Wagemaker, M.; Lafont, U.; Kelder, E. M.; Mulder, F. M. Size Effects in the $Li_{4+x}Ti_5O_{12}$ Spinel. *J. Am. Chem. Soc.* **2009**, *131*, 17786−17792.

(34) Deng, J.; Lu, Z.; Belharouak, I.; Amine, K.; Chung, C. Y. Preparation and Electrochemical Properties of $Li_4Ti_5O_{12}$ Thin Film Electrodes by Pulsed Laser Deposition. *J. Power Sources* **2009**, *193*, 816−821.

(35) Kitta, M.; Akita, T.; Maeda, Y.; Kohyama, M. Study of Surface Reaction of Spinel $Li_4Ti_5O_{12}$ During the First Lithium Insertion and Extraction Processes Using Atomic Force Microscopy and Analytical Transmission Electron Microscopy. *Langmuir* **2012**, *28*, 12384−12392.

(36) Wagemaker, M.; Simon, D. R.; Kelder, E. M.; Schoonman, J.; Ringpfeil, C.; Haake, U.; Lutzenkirchen-Hecht, D.; Frahm, R.; Mulder, F. M. A Kinetic Two-Phase and Equilibrium Solid Solution in Spinel $Li_{4+x}Ti_5O_{12}$. *Adv. Mater.* **2006**, *18*, 3169−3173.

(37) Jhan, Y.-R.; Duh, J.-G. Electrochemical Performance and Low Discharge Cut-Off Voltage Behavior of Ruthenium Doped $Li_4Ti_5O_{12}$ with Improved Energy Density. *Electrochim. Acta* **2012**, *63*, 9−15.

(38) Ouyang, C. Y.; Zhong, Z. Y.; Lei, M. S. Ab Initio Studies of Structural and Electronic Properties of $Li_4Ti_5O_{12}$ Spinel. *Electrochem. Commun.* **2007**, *9*, 1107−1112.

(39) Tsai, P.; Hsu, W. D.; Lin, S. Atomistic Structure and Ab Initio Electrochemical Properties of $Li_4Ti_5O_{12}$ Defect Spinel for Li Ion Batteries. *J. Electrochem. Soc.* **2014**, *161*, A439−A444.

(40) Jones, R. O.; Gunnarsson, O. The Density Functional Formalism, Its Applications And Prospects. *Rev. Mod. Phys.* **1989**, *61*, 689−746.

(41) Cai, R.; Jiang, S.; Yu, X.; Zhao, B.; Wang, H.; Shao, Z. A Novel Method to Enhance Rate Performance of an Al-Doped $Li_4Ti_5O_{12}$ Electrode by Post-Synthesis Treatment in Liquid Formaldehyde at Room Temperature. *J. Mater. Chem.* **2012**, *22*, 8013−8021.

(42) Bender, H.; Chen, W. D.; Portillo, J.; Van den Hove, L.; Vandervorst, W. AES and XPS Analysis of the Interaction of Ti with Si and SiO_2 during RTA. *Appl. Surf. Sci.* **1989**, *38*, 37−47.

(43) Bertoncello, R.; Casagrande, A.; Casarin, M.; Glisenti, A.; Lanzoni, E.; Mirenghi, L.; Tondello, E. Tin, Tic and Ti(C, N) Film Characterization and its Relationship to Tribological Behaviour. *Surf. Interface Anal.* **1992**, *18*, 525−531.

(44) Shi, Y.; Wen, L.; Li, F.; Cheng, H.-M. Nanosized $Li_4Ti_5O_{12}$/Graphene Hybrid Materials with Low Polarization for High Rate Lithium Ion Batteries. *J. Power Sources* **2011**, *196*, 8610−8617.

(45) Baggetto, L.; Dudney, N. J.; Veith, G. M. Surface Chemistry of Metal Oxide Coated Lithium Manganese Nickel Oxide Thin Film Cathodes Studied by XPS. *Electrochim. Acta* **2013**, *90*, 135−147.

(46) Appapillai, A. T.; Mansour, A. N.; Cho, J.; Shao-Horn, Y. Microstructure of $LiCoO_2$ with and without "$AlPO_4$" Nanoparticle Coating: Combined STEM and XPS Studies. *Chem. Mater.* **2007**, *19*, 5748−5757.

(47) He, Y. B.; Li, B. H.; Liu, M.; Zhang, C.; Lv, W.; Yang, C.; Li, J.; Du, H. D.; Zhang, B. A.; Yang, Q. H.; Kim, J. K.; Kang, F. Y. Gassing in $Li_4Ti_5O_{12}$-Based Batteries and its Remedy. *Sci. Rep.* **2012**, *2*, 913−921.

(48) He, Y.-B.; Liu, M.; Huang, Z.-D.; Zhang, B.; Yu, Y.; Li, B.; Kang, F.; Kim, J.-K. Effect of Solid Electrolyte Interface (SEI) Film on Cyclic Performance of $Li_4Ti_5O_{12}$ Anodes for Li ion Batteries. *J. Power Sources* **2013**, *239*, 269−276.

(49) Ganapathy, S.; Wagemaker, M. Nanosize Storage Properties in Spinel $Li_4Ti_5O_{12}$ Explained by Anisotropic Surface Lithium Insertion. *ACS Nano* **2012**, *6*, 8702−8712.

(50) Wang, F.; Wu, L. J.; Ma, C.; Su, D.; Zhu, Y. M.; Graetz, J. Excess Lithium Storage and Charge Compensation in Nanoscale $Li_{4+x}Ti_5O_{12}$. *Nanotechnology* **2013**, *24*, 424006.

(51) Horcas, I.; Fernandez, R.; Gomez-Rodriguez, J. M.; Colchero, J.; Gomez-Herrero, J.; Baro, A. M. WSXM: A Software for Scanning Probe Microscopy and a Tool for Nanotechnology. *Rev. Sci. Instrum.* **2007**, *78*, 013705.

(52) Kresse, G.; Furthmüller, J. Efficient Iterative Schemes for Ab Initio Total-Energy Calculations Using a Plane-Wave Basis Set. *Phys. Rev. B: Condens. Matter Mater. Phys.* **1996**, *54*, 11169−11186.

(53) Perdew, J. P.; Burke, K.; Ernzerhof, M. Generalized Gradient Approximation Made Simple. *Phys. Rev. Lett.* **1997**, *78*, 1396−1396.

(54) Kresse, G.; Furthmuller, J. Efficiency of Ab-Initio Total Energy Calculations for Metals and Semiconductors Using a Plane-Wave Basis Set. *Comput. Mater. Sci.* **1996**, *6*, 15−50.

(55) Blöchl, P. E. Projector Augmented-Wave Method. *Phys. Rev. B: Condens. Matter Mater. Phys.* **1994**, *50*, 17953−17979.

(56) Blochl, P. E.; Jepsen, O.; Andersen, O. K. Improved Tetrahedron Method For Brillouin-Zone Integrations. *Phys. Rev. B: Condens. Matter Mater. Phys.* **1994**, *49*, 16223−16233.

(57) Heyd, J.; Scuseria, G. E.; Ernzerhof, M. Hybrid Functionals Based on a Screened Coulomb Potential. *J. Chem. Phys.* **2003**, *118*, 8207−8215.

(58) Towns, J.; Cockerill, T.; Dahan, M.; Foster, I.; Gaither, K.; Grimshaw, A.; Hazlewood, V.; Lathrop, S.; Lifka, D.; Peterson, G. D.; Roskies, R.; Scott, J. R.; Wilkins-Diehr, N. XSEDE: Accelerating Scientific Discovery. *Comput. Sci. Eng.* **2014**, *16*, 62−74.